

1      **High-level cognition is supported by at least second order**  
2      **dynamic correlations in neural activity patterns**

3      Lucy L. W. Owen<sup>1</sup>, Thomas H. Chang<sup>1,2</sup>, and Jeremy R. Manning<sup>1,†</sup>

<sup>1</sup>Department of Psychological and Brain Sciences,  
Dartmouth College, Hanover, NH

<sup>3</sup>Amazon.com, Seattle, WA

<sup>†</sup>Address correspondence to jeremy.r.manning@dartmouth.edu

4      September 4, 2019

5      **Abstract**

6      Our thoughts arise from coordinated patterns of interactions between brain structures that change  
7      with our ongoing experiences. High-order dynamic correlations in brain activity patterns reflect different  
8      subgraphs of the brain’s connectome that display homologous lower-level dynamic correlations. We tested  
9      the hypothesis that high-level cognition is supported by high-order dynamic correlations in brain activity  
10     patterns. We developed an approach to estimating high-order dynamic correlations in timeseries data,  
11     and we applied the approach to neuroimaging data collected as human participants either listened to a  
12     ten-minute story or a temporally scrambled version of the story, or underwent a resting state scan. We  
13     trained across-participants pattern classifiers to decode (in held-out data) when in the session each activity  
14     snapshot was collected. We found that classifiers trained to decode from high-order dynamic correlations  
15     yielded better performance on data collected as participants listened to the (unscrambled) story. By  
16     contrast, classifiers trained to decode data from scrambled versions of the story or during the resting  
17     state scan yielded the best performance when they were trained using first-order dynamic correlations  
18     or raw activity patterns. We suggest that as our thoughts become more complex, they are supported by  
19     higher-order patterns of dynamic network interactions throughout the brain.

20     **Introduction**

21     A central goal in cognitive neuroscience is to elucidate the *neural code*: the mapping between (a) mental  
22     states or cognitive representations and (b) neural activity patterns. One means of testing models of the  
23     neural code is to ask how accurately that model is able to “translate” neural activity patterns into known  
24     (or hypothesized) mental states or cognitive representations (e.g., Haxby et al., 2001; Huth et al., 2016, 2012;  
25     Kamitani & Tong, 2005; Mitchell et al., 2008; Nishimoto et al., 2011; Norman et al., 2006; Pereira et al., 2018;  
26     Tong & Pratte, 2012). Training decoding models on different types of neural features can also help to elucidate  
27     which specific aspects of neural activity patterns are informative about cognition– and, by extension, which  
28     types of neural activity patterns might comprise the neural code. For example, prior work has used region  
29     of interest analyses to estimate the anatomical locations of specific neural representations (e.g., Etzel et al.,  
30     2009), or to compare the relative contributions to the neural code of multivariate activity patterns versus

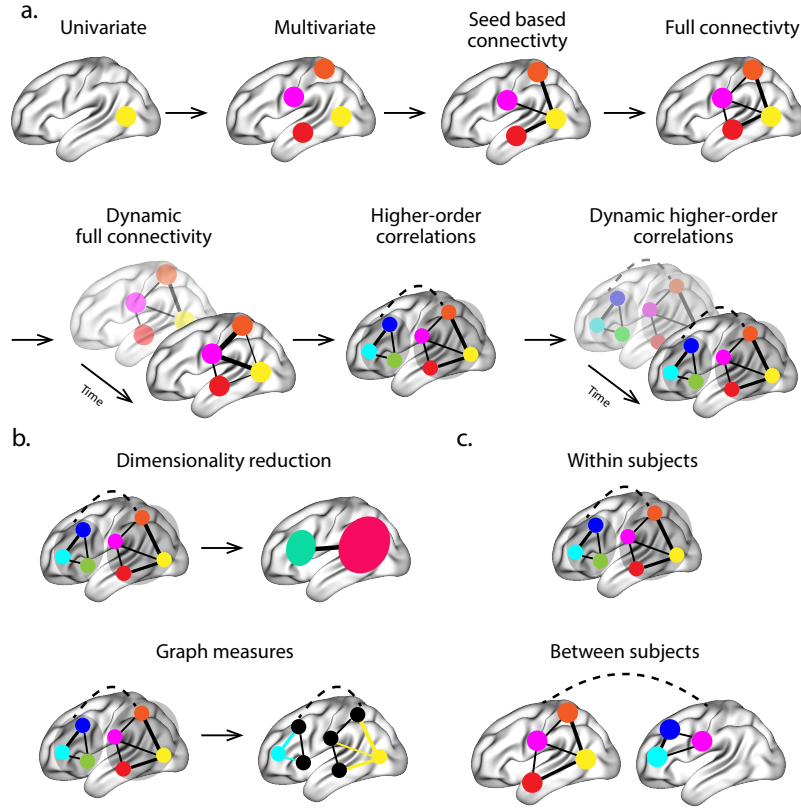


**Figure 1: Neural patterns.** The evolution of fMRI analyses started with univariate activation, which refers to the average amplitude of BOLD activity evoked by events of an experimental condition. Next, multivariate classifiers are trained on patterns of activation across voxels to decode distributed representations for specific events. The next, resting connectivity, is the temporal correlation of one or more seed regions with the remainder of the brain during rest. Additionally, task-based connectivity examines how these correlations differ by cognitive state. Following this increasing trajectory of increasing complexity, full connectivity considers all pairwise correlations in the brain, most commonly at rest. Next, dynamic full connectivity considers how full connectivity changes over time. Continuing this line of reasoning, we expect higher-order network dynamics might provide even richer insights into the neural basis of cognition.

31 patterns of dynamic correlations between neural activity patterns (e.g., Fong et al., 2019; Manning et al.,  
 32 2018). An emerging theme in this literature is that cognition is mediated by complex dynamic interactions  
 33 between brain structures (Bassett et al., 2006; Demertzi et al., 2019; Sporns & Honey, 2006; Turk-Browne,  
 34 2013).

35 Studies of the neural code to date have primarily focused on univariate or multivariate neural pat-  
 36 terns (for review see Norman et al., 2006), or (more recently) on patterns of dynamic first-order corre-  
 37 lations (i.e., interactions between pairs of brain structures; Fong et al., 2019; Manning et al., 2018). We  
 38 wondered what the future of this line of work might hold. For example, is the neural code mediated by  
 39 higher-order interactions between brain structures? Second-order correlations reflect *homologous* patterns of  
 40 correlation. In other words, if the changing patterns of correlations between two regions,  $A$  and  $B$ , are similar

41 to those between two other regions,  $C$  and  $D$ , this would be reflected in the second-order correlations be-  
42 tween ( $A-B$ ) and ( $C-D$ ). In this way, second-order correlations identify similarities and differences between  
43 subgraphs of the brain’s connectome. Analogously, third-order correlations reflect homologies between  
44 second-order correlations— i.e., homologous patterns of homologous interactions between brain regions.  
45 More generally, higher-order correlations reflect homologies between patterns of lower-order correlations.  
46 We can then ask: which “orders” of interaction are most reflective of high-level cognitive processes?

47 Another central question pertains to the extent to which the neural code is carried by activity patterns  
48 that directly reflect ongoing cognition (e.g., following Haxby et al., 2001; Norman et al., 2006), versus the  
49 dynamic properties of the network structure itself, independent of specific activity patterns in any given  
50 set of regions (e.g., following Bassett et al., 2006). For example, graph measures such as centrality and  
51 degree (Bullmore & Sporns, 2009) may be used to estimate how a given brain structure is “communicating”  
52 with other structures, independently of the specific neural representations carried by those structures.  
53 If one considers a brain region’s position in the network (e.g., its eigenvector centrality) as a dynamic  
54 property, one can compare how the positions of different regions are correlated, and/or how those patterns  
55 of correlations change over time. We can also compute higher-order patterns in these correlations to  
56 characterize homologous subgraphs in the connectome that display similar changes in their constituent  
57 brain structures’ interactions with the rest of the brain.

58 To gain insights into the above aspects of the neural code, we developed a computational framework  
59 for estimating dynamic high-order correlations in timeseries data. This framework provides an important  
60 advance, in that it enables us to examine patterns in higher-order correlations that are computationally  
61 intractable to estimate via conventional methods. Given a multivariate timeseries, our framework provides  
62 timepoint-by-timepoint estimates of the first-order correlations, second-order correlations, and so on (up to  
63 tenth-order correlations in this manuscript). Our approach combines a kernel-based method for computing  
64 dynamic correlations in timeseries data with a dimensionality reduction step that projects the resulting dy-  
65 namic correlations into a low-dimensional space. We explored two dimensionality reduction approaches:  
66 principle components analysis (PCA; Pearson, 1901), which preserves an approximately invertible transfor-  
67 mation back to the original data; and a second non-invertible algorithm that explored patterns in eigenvector  
68 centrality (Landau, 1895). This latter approach characterizes correlations between each feature dimension’s  
69 relative position in the network in favor of the specific activity histories of different features.

70 We validated our approach using synthetic data where the underlying correlations were known. We  
71 then applied our framework to a neuroimaging dataset collected as participants listened to either an audio  
72 recording of a ten-minute story or a temporally scrambled version of the story, or underwent a resting state  
73 scan (Simony et al., 2016). We used a subset of the data to train across-participant classifiers to decode

74 listening times using a blend of neural features (comprising neural activity patterns, as well as different  
75 orders of correlations between those patterns that were inferred using our computational framework).  
76 We found that both the PCA-based and eigenvector centrality-based approaches yielded neural patterns  
77 that could be used to decode accurately. Both approaches also yielded the best decoding accuracy for  
78 data collected during (intact) story listening when high-order (PCA: second-order; eigenvector centrality:  
79 fourth-order) dynamic correlation patterns were included as features. When we trained classifiers on the  
80 scrambled stories or resting state data, only lower-order dynamic patterns were informative to the decoders.  
81 Taken together, our results indicate that high-level cognition is supported by high-order dynamic patterns  
82 of communication between brain structures.

## 83 Methods

84 Our general approach to comprises four general steps (Fig. 2). First, we derive a kernel-based approach  
85 to computing dynamic pairwise correlations in a  $T$  (timepoints) by  $K$  (features) multivariate timeseries,  
86  $\mathbf{X}_0$ . This yields a  $T$  by  $O(K^2)$  matrix of dynamic correlations,  $\mathbf{Y}_1$ , where each row comprises the upper  
87 triangle of the correlation matrix at a single timepoint, reshaped into a row vector (this reshaped vector is  
88  $(\frac{K^2-K}{2})$ -dimensional). Second, we apply a dimensionality reduction step to project the matrix of dynamic  
89 correlations back onto a  $K$ -dimensional space. This yields a  $T$  by  $K$  matrix,  $\mathbf{X}_1$ , that reflects an approximation  
90 of the dynamic correlations reflected in the original data. Third, we use repeated applications of the kernel-  
91 based dynamic correlation step to  $\mathbf{X}_n$  and the dimensionality reduction step to the resulting  $\mathbf{Y}_{n+1}$  to estimate  
92 high-order dynamnic correlations. Each application of these steps to a  $T$  by  $K$  time series  $\mathbf{X}_n$  yields a  $T$  by  $K$   
93 matrix,  $\mathbf{X}_{n+1}$ , that reflects the dynamic correlations between the columns of  $\mathbf{X}_n$ . In this way, we refer to  $n$  as  
94 the *order* of the timeseries, where  $\mathbf{X}_0$  (order 0) denotes the original data and  $\mathbf{X}_n$  denotes  $n^{\text{th}}$ -order dynamic  
95 correlations between the columns of  $\mathbf{X}_0$ . Finally, we use a cross-validation-based decoding approach to  
96 evaluate how well information contained in a given order (or weighted mixture of orders) may be used  
97 to decode relevant cognitive states. If including a given  $\mathbf{X}_n$  in the feature set yields higher classification  
98 accuracy on held-out data, we interpret this as evidence that the given cognitive states are reflected in  
99 patterns of  $n^{\text{th}}$ -order correlations. All of the code used to produce the figures and results in this manuscript,  
100 along with links to the corresponding datasets, may be found at [github.com/ContextLab/timecorr-paper](https://github.com/ContextLab/timecorr-paper). In  
101 addition, we have released a Python toolbox for computing dynamic high-order correlations in timeseries  
102 data; our toolbox may be found at [timecorr.readthedocs.io](https://timecorr.readthedocs.io). **JRM NOTE: CHECK LINK**

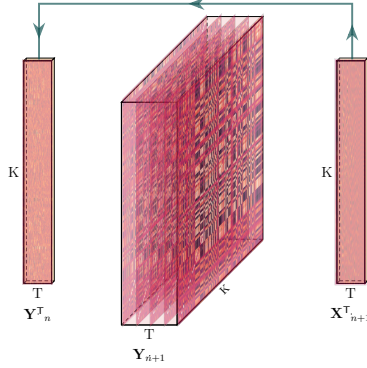


Figure 2: **Estimating dynamic high-order correlations.** Given a  $T$  by  $K$  matrix of multivariate timeseries data,  $\mathbf{Y}_n$  (where  $n \in \mathbb{N}, n \geq 0$ ), we use Equation 5 to compute a timeseries of  $K$  by  $K$  correlation matrices,  $\mathbf{Y}_{n+1}$ . We then approximate  $\mathbf{Y}_{n+1}$  with the  $T$  by  $K$  matrix  $\mathbf{X}_{n+1}$ . This process may be repeated to scalably estimate iteratively higher-order correlations in the data. Note that the transposes of  $\mathbf{Y}_n$  and  $\mathbf{X}_{n+1}$  are displayed in the figure for compactness.

### 103 Kernel-based approach for computing dynamic correlations

Given a matrix of observations, we can compute the (static) Pearson's correlation between any pair of columns,  $\mathbf{X}(\cdot, i)$  and  $\mathbf{X}(\cdot, j)$  using (Pearson, 1901):

$$\text{corr}(\mathbf{X}(\cdot, i), \mathbf{X}(\cdot, j)) = \frac{\sum_{t=1}^T (\mathbf{X}(t, i) - \bar{\mathbf{X}}(\cdot, i))(\mathbf{X}(t, j) - \bar{\mathbf{X}}(\cdot, j))}{\sqrt{\sum_{t=1}^T \sigma_{\mathbf{X}(\cdot, i)}^2 \sigma_{\mathbf{X}(\cdot, j)}^2}}, \text{ where} \quad (1)$$

$$\bar{\mathbf{X}}(\cdot, k) = \sum_{t=1}^T \mathbf{X}(t, k), \text{ and} \quad (2)$$

$$\sigma_{\mathbf{X}(\cdot, k)}^2 = \sum_{t=1}^T (\mathbf{X}(t, k) - \bar{\mathbf{X}}(\cdot, k))^2 \quad (3)$$

- 104 We can generalize this formula to compute time-varying correlations by incorporating a *kernel function* that
- 105 takes a time  $t$  as input, and returns how much the observed data at each timepoint  $\tau \in [-\infty, \infty]$  contributes
- 106 to the estimated instantaneous correlation at time  $t$  (Fig. 3).

Given a kernel function  $\kappa_t(\cdot)$  for timepoint  $t$ , evaluated at timepoints  $\tau \in [1, \dots, T]$ , we can update the

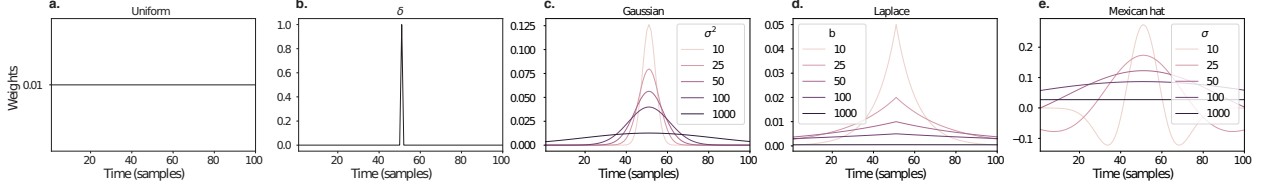


**Figure 3: Examples of kernel functions.** Each panel displays per-timepoint weights at  $t = 50$ , evaluated for 100 timepoints ( $\tau \in [1, \dots, 100]$ ). **a. Uniform kernel.** The weights are timepoint-invariant; observations at all timepoints are weighted equally, and do not change as a function of  $\tau$ . This is a special case of weight function that reduces dynamic correlations to static correlations. **b. Dirac  $\delta$  kernel.** Only the observation at timepoint  $t$  is given a non-zero weight (of 1). **c. Gaussian kernels.** Each kernel's weights fall off in time according to a Gaussian probability density function centered on time  $t$ . Weights derived using several different example width parameters ( $\sigma^2$ ) are displayed. **d. Laplace kernels.** Each kernel's weights fall off in time according to a Laplace probability density function centered on time  $t$ . Weights derived using several different example width parameters ( $b$ ) are displayed. **e. Mexican hat (Ricker wavelet) kernels.** Each kernel's weights fall off in time according to a Ricker wavelet centered on time  $t$ . This function highlights the *contrasts* between local versus surrounding activity patterns in estimating dynamic correlations. Weights derived using several different example width parameters ( $\sigma$ ) are displayed.

static correlation formula in Equation 2 to estimate the *instantaneous correlation* at timepoint  $t$ :

$$\text{timecorr}_{\kappa_t}(\mathbf{X}(\cdot, i), \mathbf{X}(\cdot, j)) = \frac{\sum_{\tau=1}^T (\mathbf{X}(\tau, i) - \tilde{\mathbf{X}}_{\kappa_t}(i))(\mathbf{X}(\tau, j) - \tilde{\mathbf{X}}_{\kappa_t}(j))}{\sqrt{\sum_{\tau=1}^T \tilde{\sigma}_{\kappa_t}^2(\mathbf{X}(\cdot, i))\tilde{\sigma}_{\kappa_t}^2(\mathbf{X}(\cdot, j))}}, \text{ where} \quad (4)$$

$$\tilde{\mathbf{X}}_{\kappa_t}(t, k) = \sum_{\tau=1}^T \kappa_t(\tau, k) \mathbf{X}(\tau, k), \quad (5)$$

$$\tilde{\sigma}_{\kappa_t}^2(\mathbf{X}(\cdot, k)) = \sum_{\tau=1}^T (\mathbf{X}(\tau, k) - \tilde{\mathbf{X}}_{\kappa_t}(t, k))^2. \quad (6)$$

107 Here  $\text{timecorr}(\mathbf{X}(\cdot, i), \mathbf{X}(\cdot, j), \kappa_t)$  reflects the correlation at time  $t$  between columns  $i$  and  $j$  of  $\mathbf{X}$ , estimated using  
 108 the kernel  $\kappa_t$ . We evaluate Equation 5 in turn each pair of columns in  $\mathbf{X}$  and for kernels centered on each  
 109 timepoint in the timeseries, respectively, to obtain a  $T$  by  $K$  by  $K$  timeseries of dynamic correlations,  $\mathbf{Y}$ . For  
 110 convenience, we then reshape the upper triangles of each timepoint's correlation matrix into a row vector  
 111 to obtain an equivalent  $T$  by  $\frac{K^2-K}{2}$  matrix.

## 112 Dynamic inter-subject functional connectivity (DISFC)

Equation 5 provides a means of taking a single observation matrix,  $\mathbf{X}_n$  and estimating the dynamic correlations from moment to moment,  $\mathbf{Y}_{n+1}$ . Suppose that one has access to a set of multiple observation matrices that reflect the same phenomenon. For example, one might collect neuroimaging data from several experimental participants, as each participant performs the same task (or sequence of tasks). Let  $\mathbf{X}_n^1, \mathbf{X}_n^2, \dots, \mathbf{X}_n^P$  reflect the  $T$  by  $K$  observation matrices ( $n = 0$ ) or reduced correlation matrices ( $n > 0$ ) for each of

$P$  participants in an experiment. We can use *inter-subject functional connectivity* (ISFC; Simony et al., 2016) to compute the degree of stimulus-driven correlations reflected in the multi-participant dataset at a given timepoint  $t$  using:

$$\bar{\mathbf{C}}(t) = M \left( R \left( \frac{1}{2P} \sum_{p=1}^P Z(Y_n^p(t))^T + Z(Y_n^p(t)) \right) \right), \quad (7)$$

where  $M$  extracts and vectorizes the diagonal and upper triangle of a symmetric matrix,  $Z$  is the Fisher z-transformation (Zar, 2010):

$$Z(r) = \frac{\log(1+r) - \log(1-r)}{2} \quad (8)$$

$R$  is the inverse of  $Z$ :

$$R(z) = \frac{\exp(2z-1)}{\exp(2z+1)}, \quad (9)$$

and  $\mathbf{Y}_n^p(t)$  denotes the correlation matrix (Eqn. 2) between each column of  $\mathbf{X}_n^p$  and each column of the average  $\mathbf{X}_n$  from all *other* participants,  $\bar{\mathbf{X}}_n^{np}$ :

$$\bar{\mathbf{X}}_n^{np} = R \left( \frac{1}{P-1} \sum_{q \in \setminus p} Z(\mathbf{X}_n^q) \right), \quad (10)$$

where  $\setminus p$  denotes the set of all participants other than participant  $p$ . In this way, the  $T$  by  $\frac{K^2-K}{2}$  DISFC matrix  $\bar{\mathbf{C}}$  provides a time-varying extension of the ISFC approach developed by Simony et al. (2016).

## 115 Low-dimensional representations of dynamic correlations

Given a  $T$  by  $\frac{K^2-K}{2}$  matrix of dynamic correlations,  $\mathbf{Y}_n$ , we propose two general approaches to computing a  $T$  by  $K$  low-dimensional representation of these correlations,  $\mathbf{X}_n$ . The first approach uses dimensionality reduction algorithms to project  $\mathbf{Y}_n$  onto a  $K$ -dimensional space. The second approach uses graph measures to characterize the relative positions of each feature ( $k \in [1, \dots, K]$ ) in the network defined by the correlation matrix at each timepoint.

### 121 Dimensionality reduction-based approaches to computing $\mathbf{X}_n$

The modern library of dimensionality reduction algorithms include Principal Components Analysis (PCA; Pearson, 1901), Probabilistic PCA (PPCA; Tipping & Bishop, 1999), Exploratory Factor Analysis (EFA;

<sup>124</sup> Spearman, 1904), Independent Components Analysis (ICA; Comon et al., 1991; Jutten & Herault, 1991),  
<sup>125</sup> *t*-Stochastic Neighbor Embedding (*t*-SNE; van der Maaten & Hinton, 2008), Uniform Manifold Approximation and Projection (UMAP; McInnes & Healy, 2018), non-negative matrix factorization (NMF; Lee &  
<sup>126</sup> Seung, 1999), Topographic Factor Analysis (TFA) Manning et al. (2014), Hierarchical Topographic Factor  
<sup>127</sup> analysis (HTFA) Manning et al. (2018), Topographic Latent Source Analysis (TLSA) Gershman et al. (2011),  
<sup>128</sup> Dictionary learning (J. Mairal et al., 2009; J. B. Mairal et al., 2009), deep autoencoders (Hinton & Salakhutdinov, 2006), among others. While complete characterizations of each of these algorithms is beyond the scope  
<sup>129</sup> of the present manuscript, the general intuition driving these approaches is to compute the  $T$  by  $I$  matrix,  
<sup>130</sup>  $\mathbf{X}$ , that is closest to the original  $T$  by  $J$  matrix,  $\mathbf{Y}$ , where (typically)  $I \ll J$ . The different approaches place  
<sup>131</sup> different constraints on what properties  $\mathbf{X}$  must satisfy and which aspects of the data are compared (and  
<sup>132</sup> how) to characterize the match between  $\mathbf{X}$  and  $\mathbf{Y}$ .

<sup>133</sup> Applying dimensionality reduction algorithms to  $\mathbf{Y}$  yields a  $\mathbf{X}$  whose columns reflect weighted combinations  
<sup>134</sup> (or nonlinear transformations) of the original columns of  $\mathbf{Y}$ . This has two main consequences. First,  
<sup>135</sup> with each repeated dimensionality reduction, the resulting  $\mathbf{X}_n$  has lower and lower fidelity (with respect to  
<sup>136</sup> what the “true”  $\mathbf{Y}_n$  might have looked like without using dimensionality reduction to maintain scalability).  
<sup>137</sup> In other words, computing  $\mathbf{X}_n$  is a lossy operation. Second, whereas each columns of  $\mathbf{Y}_n$  may always be  
<sup>138</sup> mapped directly onto specific pairs of columns of  $\mathbf{Y}_{n-1}$ , the columns of  $\mathbf{X}_n$  reflect weighted combinations  
<sup>139</sup> and/or nonlinear transformations of the columns of  $\mathbf{Y}_n$ . Many dimensionality reduction algorithms are  
<sup>140</sup> invertible (or approximately invertible). However, attempting to map a given  $\mathbf{X}_n$  back onto the original  
<sup>141</sup> feature space of  $\mathbf{Y}_0$  will usually require  $O(TK^{2n})$  space and therefore quickly becomes intractable as  $n$  or  $K$   
<sup>142</sup> grow large.

#### <sup>143</sup> **Graph measure approaches to computing $\mathbf{X}_n$**

<sup>144</sup> The above dimensionality reduction approaches to approximating a given  $\mathbf{Y}_n$  with a lower-dimensional  
<sup>145</sup>  $\mathbf{X}_n$  preserve a (potentially recombined and transformed) mapping back to the original data in  $\mathbf{Y}_0$ . We  
<sup>146</sup> also explore graph measure approaches that forgo a preserved mapping back to the original data in favor  
<sup>147</sup> of preserving each feature’s relative *position* in the broader network of interactions and connections. To  
<sup>148</sup> illustrate the distinction between the two general approaches we explore, suppose a network comprises  
<sup>149</sup> nodes  $A$ ,  $B$ , and  $C$ . If  $A$  and  $B$  exhibit uncorrelated activity patterns, the functional connection between  
<sup>150</sup> them will be (by definition) close to 0. However, if  $A$  and  $B$  each interact with  $C$  in similar ways, we might  
<sup>151</sup> attempt to capture those similarities using a measure that reflects the how  $A$  and  $B$  interact in the network.  
<sup>152</sup>

<sup>153</sup> In general, graph measures take as input a matrix of interactions (e.g., using the above notation, an  $K$

155 by  $K$  correlation matrix or binarized correlation matrix reconstituted from a single timepoint's row of  $\mathbf{Y}$ )  
156 and return as output a set of  $K$  measures describing how each node (feature) sits within that correlation  
157 matrix with respect to the rest of the population. Widely used measures include betweenness centrality (the  
158 proportion of shortest paths between each pair of nodes in the population that involves the given node in  
159 question; e.g., Barthélemy, 2004; Freeman, 1977; Geisberger et al., 2008; Newman, 2005; Opsahl et al., 2010);  
160 diversity and dissimilarity (characterizations of how differently connected a given node is from others in  
161 the population; e.g., Lin, 2009; Rao, 1982; Ricotta & Szeidl, 2006); Eigenvector centrality and pagerank  
162 centrality (measures of how influential a given node is within the broader network; e.g., Bonacich, 2007;  
163 Halu et al., 2013; Lohmann et al., 2010; Newman, 2008); transfer entropy and flow coefficients (a measure  
164 of how much information is flowing from a given node to other nodes in the network; e.g., Honey et  
165 al., 2007; Schreiber, 2000);  $k$ -coreness centrality (a measure of the connectivity of a node within its local  
166 sub-graph; e.g., Alvarez-Hamelin et al., 2005; Christakis & Fowler, 2010); within-module degree (a measure  
167 of how many connections a node has to its close neighbors in the network; e.g., Rubinov & Sporns, 2010);  
168 participation coefficient (a measure of the diversity of a node's connections to different sub-graphs in the  
169 network; e.g., Rubinov & Sporns, 2010); and sub-graph centrality (a measure of a node's participation in  
170 all of the network's sub-graphs; e.g., Estrada & Rodríguez-Velázquez, 2005); among others.

171 For a given graph measure,  $\eta : \mathbb{R}^{K \times K} \rightarrow \mathbb{R}^K$ , we can use  $\eta$  to transform each row of  $\mathbf{Y}_n$  in a way that  
172 characterizes the corresponding graph properties of each column. This results in a new  $T$  by  $K$  matrix,  $\mathbf{X}_n$ ,  
173 that reflects how the features reflected in the columns of  $\mathbf{Y}_n$  participate in the network during each timepoint  
174 (row).

## 175 Dynamic higher-order correlations

176 Because  $\mathbf{X}_n$  has the same shape as the original data  $\mathbf{X}_0$ , approximating  $\mathbf{Y}_n$  with a lower-dimensional  $\mathbf{X}_n$   
177 enables us to estimate high-order dynamic correlations in a scalable way. Given a  $T$  by  $K$  input matrix, the  
178 output of Equation 5 requires  $O(TK^2)$  space to store. Repeated applications of Equation 5 (i.e., computing  
179 dynamic correlations between the columns of the outputted dynamic correlation matrix) each require  
180 exponentially more space; in general the  $n^{\text{th}}$ -order dynamic correlations of a  $T$  by  $K$  timeseries occupies  
181  $O(TK^{2n})$  space. However, when we approximate or summarize the output of Equation 5 with a  $T$  by  $K$  matrix  
182 (as described above), it becomes feasible to compute even very high-order correlations in high-dimensional  
183 data. Specifically, approximating the  $n^{\text{th}}$ -order dynamic correlations of a  $T$  by  $K$  timeseries requires only  
184  $O(TK^2)$  additional space— the same as would be required to compute first-order dynamic correlations. In  
185 other words, the space required to store  $n + 1$  multivariate timeseries reflecting up to  $n^{\text{th}}$  order correlations

186 in the original data scales linearly with  $n$  using our approach (Fig. 2).

## 187 Data

188 We examined two types of data: synthetic data and human functional neuroimaging data. We constructed  
189 and leveraged the synthetic data to evaluate our general approach. Specifically, we tested how well  
190 Equation 5 could be used to recover known dynamic correlations using different choices of kernel ( $\kappa$ ; Fig. 3),  
191 for each of several synthetic datasets that exhibited different temporal properties. We applied our approach  
192 to a functional neuroimaging dataset to test the hypothesis that ongoing cognitive processing is reflected  
193 in high-order dynamic correlations. We used an across-participant classification test to estimate whether  
194 dynamic correlations of different orders contain information about which timepoint in a story participants  
195 were listening to.

### 196 Synthetic data

197 We constructed a total of 40 multivariate timeseries, collectively reflecting a total of 4 different patterns of  
198 dynamic correlations (i.e., 10 datasets reflecting each type of dynamic pattern). Each timeseries comprised  
199 50 features (dimensions) that varied over 300 timepoints. The observations at each timepoint were drawn  
200 from a zero-mean multivariate Gaussian distribution with a covariance matrix defined for each timepoint  
201 as described below. We drew the observations at each timepoint independently from the draws at all other  
202 timepoints; in other words, for each observation  $s_t \sim \mathcal{N}(\mathbf{0}, \Sigma_t)$  at timepoint  $t$ ,  $p(s_t) = p(s_t | p_{\setminus t})$ .

**Constant.** We generated data with stable underlying correlations to evaluate how Equation 5 characterized correlation “dynamics” when the ground truth correlations were static. We constructed 10 multivariate timeseries, whose observations were each drawn from a single (stable) Gaussian distribution. For each dataset, we constructed a random covariance matrix,  $\Sigma_m$ :

$$\mathbf{C}(i, j) \sim \mathcal{N}(0, 1) \tag{11}$$

$$\Sigma_m = \mathbf{C}\mathbf{C}^\top, \text{ where} \tag{12}$$

203  $i, j \in [1, 2, \dots, 50]$ . In other words, all of the observations (for each of the 300 timepoints) within each dataset  
204 were drawn from a multivariate Gaussian distribution with the same covariance matrix, and the 10 datasets  
205 each used a different covariance matrix.

206 **Random.** We generated a second set of 10 synthetic datasets whose observations at each timepoint were  
207 drawn from a Gaussian distribution with a new randomly constructed (using Eqn. 12) covariance matrix.  
208 Because each timepoint’s covariance matrix was drawn independently of the covariance matrices for all  
209 other timepoints, these datasets provided a test of reconstruction accuracy in the absence of any meaningful  
210 underlying temporal structure in the dynamic correlations underlying the data.

**Ramping.** We generated a third set of 10 synthetic datasets whose underlying correlations changed gradually over time. For each dataset, we constructed two *anchor* correlation matrices using Equation 12,  $\Sigma_{\text{start}}$  and  $\Sigma_{\text{end}}$ . For each of the 300 timepoints in each dataset, we drew the observations from a multivariate Gaussian distribution whose covariance matrix at each timepoint  $t \in [0, \dots, 299]$  was given by

$$\Sigma_t = \left(1 - \frac{1-t}{299}\right)\Sigma_{\text{start}} + \frac{t}{299}\Sigma_{\text{end}}. \quad (13)$$

211 The gradually changing correlations underlying these datasets allow us to evaluate the recovery of dynamic  
212 correlations when each timepoint’s correlation matrix is unique (as in the random datasets), but where the  
213 correlation dynamics are structured.

214 **Event.** We generated a fourth set of 10 synthetic datasets whose underlying correlation matrices exhibited  
215 prolonged intervals of stability, interspersed with abrupt changes. For each dataset, we used Equation ??  
216 to generate 5 random covariance matrices. We constructed a timeseries where each set of 60 consecutive  
217 samples was drawn from a Gaussian with the same covariance matrix. These datasets were intended to  
218 simulate a system that undergoes occasional abrupt state changes.

## 219 Functional neuroimaging data collected during story listening

220 We examined an fMRI dataset collected by Simony et al. (2016) that the authors have made publically  
221 available at [arks.princeton.edu/ark:/88435/dsp015d86p269k](http://arks.princeton.edu/ark:/88435/dsp015d86p269k). The dataset comprises neuroimaging data  
222 collected as participants listened to an audio recording of a story (intact condition; 36 participants), listened  
223 to time scrambled recordings of the same story (17 participants in the paragraph-scrambled condition  
224 listened to the paragraphs in a randomized order and 36 in the word-scrambled condition listened to  
225 the words in a randomized order), or lay resting with their eyes open in the scanner (rest condition; 36  
226 participants). Full neuroimaging details may be found in the original paper for which the data were  
227 collected (Simony et al., 2016).

228 **Hierarchical topographic factor analysis (HTFA).** Following our prior related work, we used HTFA (Manning et al., 2018) to derive a compact representation of the data. In brief, this approach approximates the  
229 timeseries of voxel activations (44,415 voxels) using a much smaller number of radial basis function (RBF)  
230 nodes (in this case 700 nodes). This provides a convenient representation for examining full-brain network  
231 dynamics. All of the analyses we carried out on the neuroimaging dataset were performed in this lower-  
232 dimensional space. In other words, each participant’s data matrix,  $Y_0$ , was a number-of-timepoints by 700  
233 matrix of HTFA-derived factor weights (where the row and column labels were matched across partici-  
234 pants). Code for carrying out HTFA on fMRI data may be found as part of the BrainIAK toolbox (Capota et  
235 al., 2017), which may be downloaded at [brainiak.org](http://brainiak.org).

## 237 **Temporal decoding**

238 We sought to identify neural patterns that reflected participants’ ongoing cognitive processing of incoming  
239 stimulus information. As reviewed by Simony et al. (2016), one way of homing in on these stimulus-driven  
240 neural patterns is to compare activity patterns across individuals (e.g., using ISFC analyses). In particular,  
241 neural patterns will be similar across individuals, to the extent that the neural patterns under consideration  
242 are stimulus driven, and to the extent that the corresponding cognitive representations are reflected in similar  
243 spatial patterns across people. Following this logic, we used an across-participants temporal decoding test  
244 developed by Manning et al. (2018) to assess the degree to which different neural patterns reflected ongoing  
245 stimulus-driven cognitive processing across people. The approach entails using a subset of the data to  
246 train a classifier to decode which stimulus timepoint (i.e., moment in the story participants listened to). We  
247 use decoding (forward inference) accuracy on held-out data, from held-out participants, as a proxy for the  
248 extent to which the inputted neural patterns reflected stimulus-driven cognitive processing in a similar way  
249 across individuals.

## 250 **Forward inference and decoding accuracy**

251 We used an across-participants correlation-based classifier to decode which stimulus timepoint matched a  
252 given neural pattern. We first divided the participants into two groups: a template group,  $\mathcal{G}_{\text{template}}$ , and a  
253 to-be-decoded group,  $\mathcal{G}_{\text{decode}}$ . We used Equation 7 to compute a DISFC matrix for each group ( $\bar{\mathbf{C}}_{\text{template}}$  and  
254  $\bar{\mathbf{C}}_{\text{decode}}$ , respectively). We then correlated the rows of  $\bar{\mathbf{C}}_{\text{template}}$  and  $\bar{\mathbf{C}}_{\text{decode}}$  to form a number-of-timepoints by  
255 number-of-timepoints decoding matrix,  $\Lambda$ . In this way, the rows of  $\Lambda$  reflected timepoints from the template  
256 group, while the columns reflected timepoints from the to-be-decoded group. We assigned temporal labels  
257 to each row  $\bar{\mathbf{C}}_{\text{decode}}$  using the row of  $\bar{\mathbf{C}}_{\text{template}}$  to which it was most highly correlated. We then repeated

258 this decoding procedure, but using  $\mathcal{G}_{\text{decode}}$  as the template group and  $\mathcal{G}_{\text{template}}$  as the to-be-decoded group.  
259 Given the true timepoint labels (for each group), we defined the *decoding accuracy* as the proportion of  
260 correctly decoded timepoints, across both groups.

261 **Feature weighting and testing**

262 We sought to examine which types of neural features (i.e., activations, first-order dynamic correlations, and  
263 higher-order dynamic correlations) were informative to the temporal decoders. Using the notation above,  
264 these features correspond to  $\mathbf{Y}_0, \mathbf{X}_1, \mathbf{X}_2, \mathbf{X}_3$ , and so on (we examined up to tenth order correlations, or  $\mathbf{X}_{10}$ ).

265 One challenge to fairly evaluating high-order correlations is that if the kernel used in Equation 5 is  
266 wider than a single timepoint, each repeated application of the equation will result in further temporal  
267 blur. Because our primary assessment metric is temporal decoding accuracy, this unfairly biases against  
268 detecting meaningful signal in higher-order correlations (relative to lower-order correlations). We attempted  
269 to mitigate temporal blur in estimating each  $\mathbf{X}_n$  by using a Dirac  $\delta$  function kernel (which places all of its  
270 mass over a single timepoint; Fig. 3b) to compute each lower-order correlation ( $\mathbf{X}_1, \mathbf{X}_2, \dots, \mathbf{X}_{n-1}$ ). We then used  
271 a (potentially wider, as described below) kernel to compute  $\mathbf{X}_n$  from  $\mathbf{X}_{n-1}$ . In this way, temporal blurring  
272 was applied only in the last step of computing  $\mathbf{X}_n$ . We note that, because each  $\mathbf{X}_n$  is a low-dimensional  
273 representation of the corresponding  $\mathbf{Y}_n$ , the higher-order correlations we estimated reflect true correlations  
274 in the data with lower-fidelity than estimates of lower-order correlations.

275 After computing each  $\mathbf{X}_1, \mathbf{X}_2, \dots, \mathbf{X}_{n-1}$  for each participant, we divided participants into two equally sized  
276 groups ( $\pm 1$  for odd numbers of participants):  $\mathcal{G}_{\text{train}}$  and  $\mathcal{G}_{\text{test}}$ . We then further subdivided  $\mathcal{G}_{\text{train}}$  into  $\mathcal{G}_{\text{train}_1}$   
277 and  $\mathcal{G}_{\text{train}_2}$ . We then computed  $\Lambda$  temporal correlation matrices for each type of neural feature, using  $\mathcal{G}_{\text{train}_1}$   
278 and  $\mathcal{G}_{\text{train}_2}$ . This resulted in  $n + 1$   $\Lambda$  matrices (one for the original timeseries of neural activations, and one  
279 for each of  $n$  orders of dynamic correlations). Our objective was to find a set of weights of each of these  $\Lambda$   
280 matrices such that the weighted average of the  $n + 1$  matrices yielded the highest decoding accuracy. We  
281 used quasi-Newton gradient ascent (Nocedal & Wright, 2006), using decoding accuracy as the objective  
282 function to be maximized, to find an optimal set of training data-derived weights,  $\phi_{0,1,\dots,n}$ , where  $\sum_{i=0}^n \phi_i = 1$   
283 and where  $\phi_i \geq 0 \forall i \in [0, 1, \dots, n]$ .

284 After estimating an optimal set of weights, we computed a new set of  $n + 1$   $\Lambda$  matrices correlating the  
285 DISFC patterns from  $\mathcal{G}_{\text{train}}$  and  $\mathcal{G}_{\text{test}}$  at each timepoint. We use the resulting decoding accuracy of  $\mathcal{G}_{\text{test}}$   
286 timepoints to estimate how informative the set up neural features containing up to  $n^{\text{th}}$  order correlations  
287 were.

288 We used a permutation-based procedure to form a stable estimate of decoding accuracy for each set of

289 neural features. In particular, we computed the decoding accuracy for each of 10 random group assignments  
290 of  $\mathcal{G}_{\text{train}}$  and  $\mathcal{G}_{\text{test}}$ . We report the mean accuracy (and 95% confidence intervals) for each set of neural features.

291 **Identifying robust decoding results**

292 The temporal decoding procedure we use to estimate which neural features support ongoing cognitive  
293 processing is governed by many parameters. For example, Equation 5 requires defining a kernel function,  
294 which can take on different shapes and widths. For a fixed set of neural features, each of these parameters  
295 can yield different decoding accuracies. Further, the best decoding accuracy for a given timepoint may be  
296 reliably achieved by one set of parameters, whereas the best decoding accuracy for another timepoint might  
297 be reliably achieved by a different set of parameters, and the best decoding accuracy across *all* timepoints  
298 might be reliably achieved by still another different set of parameters. Rather than attempting to maximize  
299 decoding accuracy, we sought to discover the trends in the data that were robust to specific classifier  
300 parameters choices. Specifically, we sought to characterize how decoding accuracy varied (under different  
301 experimental conditions) as a function of which neural features were considered.

302 To identify decoding results that were robust to specific classifier parameter choices, we repeated our  
303 decoding analyses that substituted in a variety of kernel shapes and widths for Equation 5. We examined  
304 Gaussian (Fig. 3c), Laplace (Fig. 3d), and Mexican Hat (Fig. 3e) kernels, each with widths of 5, 10, 20, and  
305 50 samples. We then report the average decoding accuracies across all of these parameter choices. This  
306 enabled us to (roughly) factor out performance characteristics that were parameter dependent (within the  
307 space of parameters we examined).

308 **Reverse inference**

309 The dynamic patterns we examine comprise high-dimensional correlation patterns at each timepoint. To  
310 help interpret the resulting patterns in the context of other studies, we created summary maps by computing  
311 the across-timepoint average pairwise correlations at each order of analysis (first order, second order, etc.,  
312 up to fifteenth order correlations). We selected the 10 strongest (absolute value) correlations at each order.  
313 Each correlation is between the dynamic activity patterns (or patterns of dynamic high-order correlations)  
314 measured at two RBF nodes (see *Hierarchical Topographic Factor Analysis*). Therefore, the 10 strongest  
315 correlations involved up to 20 RBF nodes. Each RBF defines a spatial function whose activations range  
316 from 0 to 1. We thresholded each RBF at 0.999 to construct a map of spherical components that denoted the  
317 endpoints of the 10 strongest correlations. We then carried out a meta analysis using Neurosynth (Rubin et  
318 al., 2017) to identify the 10 terms most commonly associated with the given map. This resulted in a set of

319 10 terms associated with the average dynamic correlation patterns at each order.

## 320 Results

321 We sought to understand whether high-level cognition is supported by dynamic patterns of high-order  
322 correlations. To that end, we developed a computational framework for estimating the dynamics of high-  
323 order correlations in multivariate timeseries data (see *Dynamic inter-subject functional connectivity (DISFC)*  
324 and *Dynamic higher-order correlations*). We evaluated the efficacy of this framework at recovering known  
325 patterns in several synthetic datasets (see *Synthetic data*). We then applied the framework to a public fMRI  
326 dataset collected as participants listened to an auditorily presented story, a temporally scrambled version  
327 of the story, or underwent a resting state scan (see *Functional neuroimaging data collected during story listening*).  
328 We used the relative decoding accuracies of classifiers trained on different sets of neural features to estimate  
329 which types of features reflected ongoing cognitive processing.

### 330 Recovering known dynamic correlations from synthetic data

331 We generated synthetic datasets that differed in how the underlying correlations changed over time. For  
332 each dataset, we applied Equation 5 with a variety of kernel shapes and widths. We assessed how well  
333 the true underlying correlations at each timepoint matched the recovered correlations (Fig. 4). For every  
334 kernel and dataset we tested, our approach recovered the correlation dynamics we embedded into the data.  
335 However, the quality of these recoveries varied across different synthetic datasets in a kernel-dependent  
336 way.

337 In general, wide monotonic kernels (Laplace, Gaussian) performed best when the correlations varied  
338 gradually from moment-to-moment (Figs. 4a, c, and d). **TODO: Say something about kernel widths within**  
339 **a shape.** In the extreme, as the rate of change in correlations approaches 0 (Fig. 4a), an infinitely wide kernel  
340 would exactly recover the Pearson's correlation (e.g., compare Eqns. 2 and 5).

341 When the correlation dynamics were unstructured in time (Fig. 4b), a Dirac  $\delta$  kernel (infinitely narrow)  
342 performed best. This is because, when every timepoint's correlations are independent of the correlations in  
343 every other timepoint, averaging data over time dilutes the available signal. **TODO: Say something about**  
344 **kernel widths within a shape.**

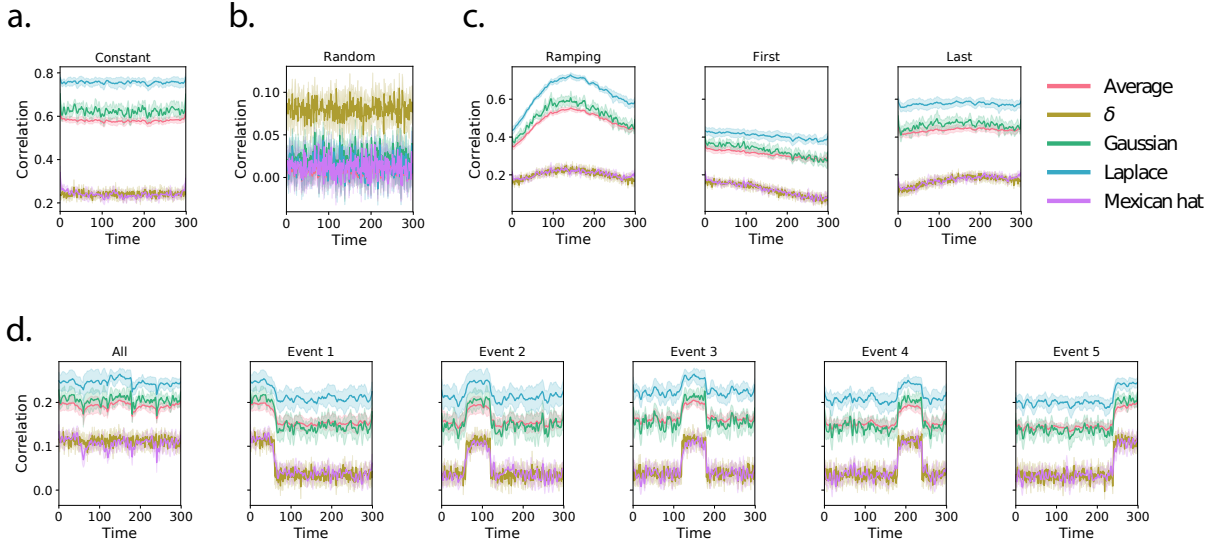


**Figure 4: Recovering known dynamic correlations from synthetic data.** Each panel displays the average correlations between the vectorized upper triangles of the recovered correlation matrix at each timepoint and either the true underlying correlation at each timepoint or a reference correlation matrix. (The averages are taken across 10 different randomly generated synthetic datasets of the given category.) Error ribbons denote 95% confidence intervals (taken across datasets). Different colors denote different kernel shapes, whereas the shading within each color type denotes kernel widths. For a complete description of each synthetic dataset, see *Synthetic data*. **a. Constant correlations.** These datasets have a stable (unchanging) underlying correlation matrix. **b. Random correlations.** These datasets are generated using a new independently drawn correlation matrix at each new timepoint. **c. Ramping correlations.** These datasets are generated by smoothly varying the underlying correlations between the randomly drawn correlation matrices at first and last timepoints. The left panel displays the correlations between the recovered dynamic correlations and the underlying ground truth correlations. The middle panel compares the recovered correlations with the *first* timepoint’s correlation matrix. The right panel compares the recovered correlations with the *last* timepoint’s correlation matrix. **d. Event-based correlations.** These datasets are each generated using five randomly drawn correlation matrices that each remain stable for a fifth of the total timecourse. The left panel displays the correlations between the recovered dynamic correlations and the underlying ground truth correlations. The right panels compare the recovered correlations with the correlation matrices unique to each event.

345 **Cognitively relevant dynamic high-order correlations in fMRI data**

346 We used across-participant temporal decoders to identify cognitively relevant neural patterns in fMRI data  
347 (see *Forward inference and decoding accuracy*). The dataset we examined (collected by Simony et al., 2016)  
348 comprised four experimental conditions that exposed participants to stimuli that varied systematically in  
349 how cognitively engaging they were. The *intact* experimental condition had participants listen to an audio  
350 recording of a 10-minute story. The *paragraph*-scrambled experimental condition had participants listen to a  
351 temporally scrambled version of the story, where the paragraphs occurred out of order (but where the same  
352 total set of paragraphs were presented over the full listening interval). All participants in this condition  
353 experienced the scrambled paragraphs in the same order. The *word*-scrambled experimental condition had  
354 participants listen to a temporally scrambled version of the story where the words in the story occurred in a  
355 random order. All participants in the word conditions experienced the scrambled words in the same order.  
356 Finally, in a *rest* experimental condition participants lay in the scanner with no overt stimulus, with their  
357 eyes open (blinking as needed). This dataset provided a convenient means of testing our hypothesis that  
358 different levels of cognitive engagement might be supported by different orders of complex brain activity  
359 dynamics.

360 In brief, we computed timeseries of dynamic high-order correlations that were similar across participants  
361 in each of two randomly assigned groups: a training group and a test group. We then trained classifiers  
362 on the training group's data to match each sample from the test group with a stimulus timepoint. Each  
363 classifier comprised a weighted blend of neural patterns that reflected up to  $n^{\text{th}}$ -order dynamic correlations  
364 (see *Feature weighting and testing*). We repeated this process for  $n \in \{0, 1, 2, \dots, 10\}$ . Our examinations of  
365 synthetic data suggested that none of the kernels we examined were "universal" in the sense of optimally  
366 recovering underlying correlations regardless of the structure of those correlations. In our analyses of neural  
367 data, we therefore averaged our decoding results over a variety of kernel shapes and widths in order to  
368 identify results that were robust to specific kernel parameters (also see *Identifying robust decoding results*).

369 Our approach to estimating dynamic high-order correlations requires mapping the high-dimensional  
370 feature space of correlations (a  $T$  by  $O(K^2)$  matrix) onto a lower-dimensional  $T$  by  $K$  matrix. We carried out  
371 two sets of analyses that differed in how this mapping was computed. The first set of analyses used PCA  
372 to find a low-dimensional embedding of the original dynamic correlation matrices (Fig. 5a,b). The second  
373 set of analyses characterized correlations in dynamics of each feature's eigenvector centrality, but did not  
374 preserve the underlying activity dynamics (Fig. 5c,d).

375 Both sets of temporal decoding analyses yielded qualitatively similar results for the auditory (non-  
376 rest) conditions of the experiment (Fig. 5: pink, yellow, and teal lines). The highest decoding accuracy

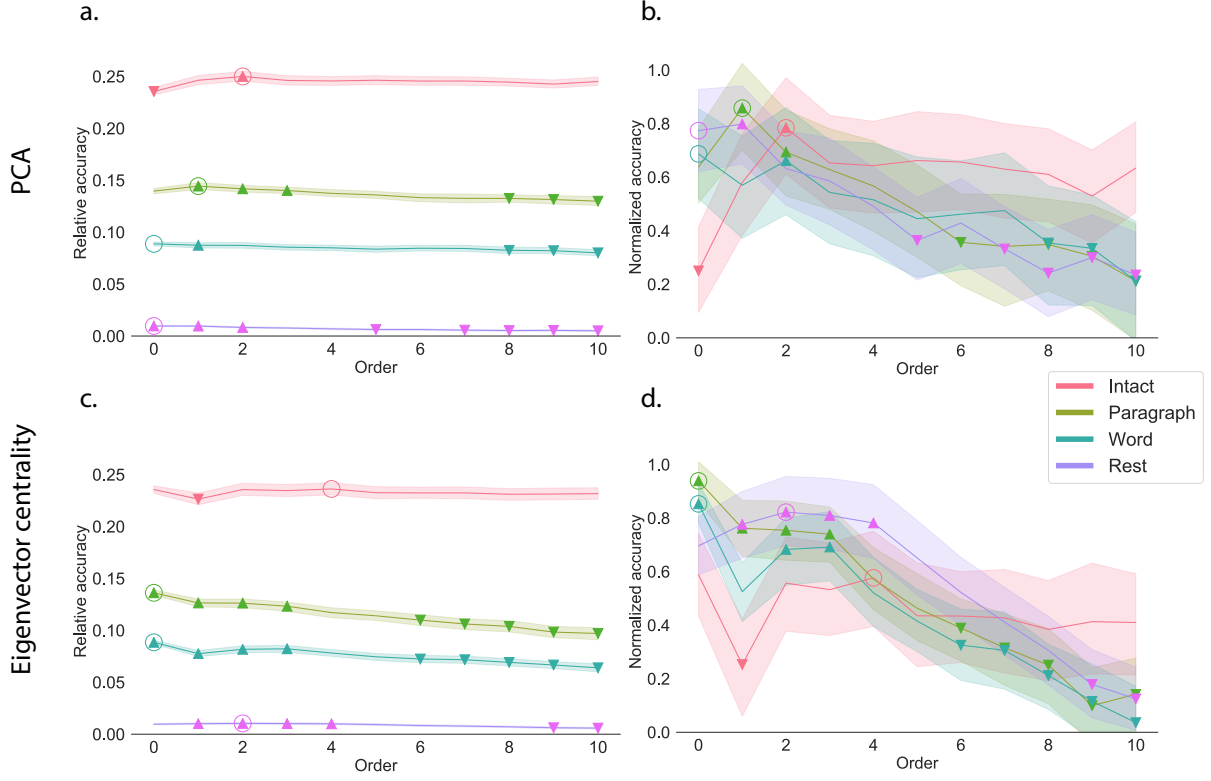


**Figure 5: Across-participant decoding accuracy varies with correlation order and cognitive engagement.**

**a. Decoding accuracy as a function of order: PCA.** Order (x-axis) refers to the maximum order of dynamic correlations that were available to the classifiers (see *Feature weighting and testing*). The reported across-participant decoding accuracies are averaged over all kernel shapes and widths (see *Identifying robust decoding results*). The y-values are displayed relative to chance accuracy (intact:  $\frac{1}{300}$ ; paragraph:  $\frac{1}{272}$ ; word:  $\frac{1}{300}$ ; rest:  $\frac{1}{400}$ ). The error bars denote 95% confidence intervals across cross-validation folds (i.e., random assignments of participants to the training and test sets). The colors denote the experimental condition. Arrows denote sets of features that yielded reliably higher (upwards facing) or lower (downward facing) decoding accuracy than the mean of all other features (via a two-tailed test, thresholded at  $p < 0.05$ ). The circled values represent the maximum decoding accuracy within each experimental condition.

**b. Normalized decoding accuracy as a function of order: PCA.** This panel displays the same results as Panel a, but here each curve has been normalized to have a maximum value of 1 and a minimum value of 0 (including the upper and lower bounds of the respective 95% confidence intervals). Panels a and b used PCA to project each high-dimensional pattern of dynamic correlations onto a lower-dimensional space.

**c. Decoding accuracy as a function of order: eigenvector centrality.** This panel is in the same format as Panel a, but here eigenvector centrality has been used to project the high-dimensional patterns of dynamic correlations onto a lower-dimensional space.

**d. Normalized decoding accuracy as a function of order: eigenvector centrality.** This panel is in the same format as Panel b, but here eigenvector centrality has been used to project the high-dimensional patterns of dynamic correlations onto a lower-dimensional space.

377 for participants who listened to the intact (unscrambled) story was achieved using high-order dynamic  
378 correlations (PCA: second-order; eigenvector-centrality: fourth-order). Scrambled versions of the story were  
379 best decoded by lower-order correlations (PCA/paragraph: first-order; PCA/word: order zero; eigenvector  
380 centrality/paragraph: order zero; eigenvector centrality/word: order zero). The two sets of analyses yielded  
381 different decoding results on resting state data (Fig. 5: purple lines). We note could be decoded only very  
382 slightly above chance; we speculate that the decoders might have picked up on attentional drift, boredom,  
383 or tiredness; we hypothesize these all increase throughout the resting state scan. Our decoders might  
384 be picking up on aspects of these loosely defined cognitive states that are common across individuals. The  
385 PCA-based approach achieved the highest resting state decoding accuracy using order zero features (non-  
386 correlational activation-based), whereas the eigenvector centrality-based approach achieved the highest  
387 resting state decoding accuracy using second-order correlations. Taken together, these analyses indicate  
388 that high-level cognitive processing (while listening to the intact story) is reflected in the dynamics of high-  
389 order correlations in brain activity, whereas lower-level cognitive processing (while listening to scrambled  
390 versions of the story that lack rich meaning) is reflected in the dynamics of lower-order correlations and  
391 non-correlational activity dynamics. Further, these patterns are associated both with the underlying activity  
392 patterns (characterized using PCA) and also with the changing relative positions that different brain areas  
393 occupy in their associated networks (characterized using eigenvector centrality).

394 Having established that patterns of high-order correlations are informative to decoders, we next won-  
395 dered which specific networks of brain regions contributed most to these patterns. As a representative  
396 example, we selected the kernel parameters that yielded decoding accuracies that best matched the average  
397 accuracies across all of the kernel parameters we examined. Using Figure ??c as a template, the best-  
398 matching kernel was a Laplace kernel with a width of 50 (Fig. 3d). We used this kernel to compute a single  
399  $K$  by  $K$   $n^{\text{th}}$ -order correlation matrix for each experimental condition, along with the Neurosynth (Rubin et  
400 al., 2017) terms most highly associated with each of these matrices (Fig. 6; see *Reverse inference*).

401 For all of the story listening conditions (intact, paragraph, and word), we found that first- and second-  
402 order correlations were most strongly associated with auditory and speech processing. During intact story  
403 listening, third-order correlations reflected integration with visual areas, and fourth-order correlations  
404 reflected integration with areas associated with high-level cognition and cognitive control, such as the ven-  
405 tralateral prefrontal cortex. However, during listening to temporally scrambled stories, these higher-order  
406 correlations instead involved interactions with additional regions associated with speech and semantic pro-  
407 cessing. By contrast, we found a much different set of patterns in the resting state data. First-order resting  
408 state correlations were most strongly associated with regions involved in counting and numerical under-  
409 standing. Second-order resting state correlations were strongest in visual areas; third-order correlations

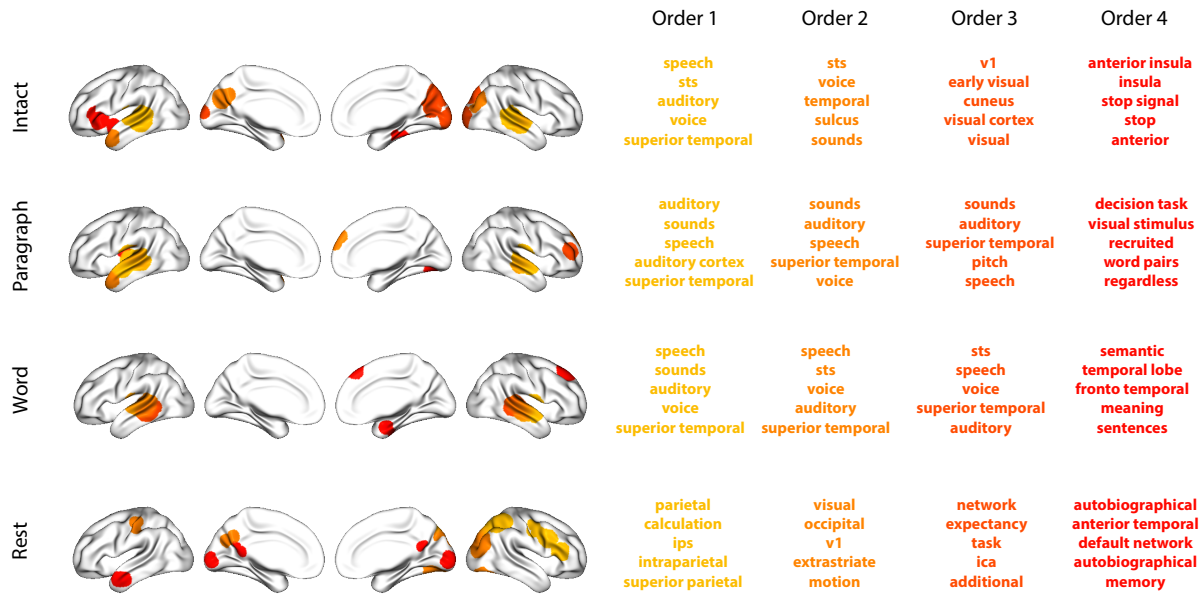


**Figure 6: Top terms associated with the endpoints of the strongest correlations.** Each color corresponds to one order of correlations, averaged across participants and time. The inflated brain plots display the locations of the endpoints of the 10 strongest (absolute value) correlations at each order, projected onto the cortical surface (Combrisson et al., 2019). The lists of terms on the right display the top five Neurosynth terms (Rubin et al., 2017) decoded from the corresponding brain maps for each order. Each row displays data from a different experimental condition. Additional maps and their corresponding Neurosynth terms may be found in the *Supplementary materials* (intact: Figure S1; paragraph: Figure S2; word: Figure S3; rest: Figure S4).

410 were strongest in task-positive areas; and fourth-order correlations were strongest in regions associated  
411 with autobiographical and episodic memory. We carried out analogous analyses to create maps (and de-  
412 code the top associated Neurosynth terms) for up to fifteenth-order correlations (Figs. S1, S2, S3, and S4).  
413 Of note, examining fifteenth-order correlations between 700 nodes using conventional methods would have  
414 required storing roughly  $\frac{700^{2 \times 15}}{2} \approx 1.13 \times 10^{85}$  floating point numbers—assuming single-precision (32 bits  
415 each), this would require roughly 32 times as many bits as there are molecules in the known universe!  
416 Although these fifteenth-order correlations do appear (visually) to have some well-formed structure, we  
417 provide this latter example primarily as a demonstration of the efficiency and scalability of our approach.

418 **JRM STOPPED HERE**

## 419 Discussion

- 420 • Methods advances: kernel-based dynamic correlations, extension to dynamic ISFC, efficient method  
421 for estimating high-order dynamic correlations, identifying robust results by averaging
- 422 • Discoveries:
  - 423 – Dimensionality reduction and graph theoretic approaches give different insights into the data  
424 and identify different patterns as being relevant to cognition (different peak orders).
  - 425 – An insight common to both approaches is that high-order (greater than first order) dynamic  
426 correlations are informative about ongoing high-level cognitive processing. As the level of  
427 cognitive processing decreases, cognition is reflected by lower-order correlations.
  - 428 – Correlations at different orders are also associated with different networks of brain regions. How-  
429 ever, which networks reflect which types of interactions depends on the current task. In general,  
430 lower order correlations during auditory listening reflect processing of low-level (auditory) fea-  
431 tures; mid-order correlations reflect speech and linguistic processing; higher-order correlations  
432 reflect across-sensory integration (e.g. ties to visual areas) and cognitive control areas. This  
433 hierarchy dissolves during lower-order cognitive processing.

434 Based on prior work (Demertzis et al., 2019) and following the direction of the field (Turk-Browne, 2013)  
435 we think our thoughts might be encoded in dynamic network patterns, and possibly higher order network  
436 patterns (Fig. 1). We sought to test this hypothesis by developing an approach to inferring high-order  
437 network dynamics from timeseries data.

438 One challenge in studying dynamic interactions is the computational resources required to calculate  
439 higher-order correlations. We developed a computationally tractable model of network dynamics (Fig. 2)

440 that takes in a feature timeseries and outputs approximated first-order dynamics (i.e., dynamic functional  
441 correlations), second-order dynamics (reflecting homologous networks that dynamically form and disperse),  
442 and higher-order network dynamics (up to tenth-order dynamic correlations).

443 We first validated our model using synthetic data, and explored how recovery varied with different  
444 underlying data structures and kernels. We then applied the approach to an fMRI dataset (Simony et al.,  
445 2016) in which participants listened to an audio recording of a story, as well as scrambled versions of the  
446 same story (where the scrambling was applied at different temporal scales). We trained classifiers to take  
447 the output of the model and decode the timepoint in the story (or scrambled story) that the participants  
448 were listening to. We found that, during the intact listening condition in the experiment, classifiers that  
449 incorporated higher-order correlations yielded consistently higher accuracy than classifiers trained only  
450 on lower-order patterns (Fig. ??, a.&d.). By contrast, these higher-order correlations were not necessary  
451 to support decoding the other listening conditions and (minimally above chance) during a control rest  
452 condition. This suggests that the cognitive processing that supported the most cognitively rich listening  
453 conditions involved second-order (or higher) network dynamics.

454 Although we found decoding accuracy was best when incorporating higher-order network dynamics  
455 for all but rest condition, it is unclear if this is a product of the brain or the data collection technique. It could  
456 be that the brain is second-order or it could be that fMRI can only reliably give second-order interactions.  
457 Exploring this method with other data collection technique will be important to disentangle this question.

## 458 **Concluding remarks**

459 How can we better understand how brain patterns change over time? How can we quantify the potential  
460 network dynamics that might be driving these changes? One way to judge the techniques of the future is  
461 to look at the trajectory of the fMRI field so far has taken so far (Fig. 2). The field started with univariate  
462 activation, measuring the average activity for each voxel. Analyses of multivariate activation followed,  
463 looking at spatial patterns of activity over voxels. Next, correlations of activity were explored, first with  
464 measures like resting connectivity that take temporal correlation between a seed voxel and all other voxels  
465 then with full connectivity that measure all pairwise correlations. Additionally, this path of increasing  
466 complexity also moved from static to dynamic measurements. One logical next step in this trajectory would  
467 be dynamic higher-order correlations. We have created a method to support these calculations by scalably  
468 approximating dynamic higher-order correlations.

469 **Acknowledgements**

470 We acknowledge discussions with Luke Chang, Hany Farid, Paxton Fitzpatrick, Andrew Heusser, Eshin  
471 Jolly, Qiang Liu, Matthijs van der Meer, Judith Mildner, Gina Notaro, Stephen Satterthwaite, Emily Whitaker,  
472 Weizhen Xie, and Kirsten Ziman. Our work was supported in part by NSF EPSCoR Award Number 1632738  
473 to J.R.M. and by a sub-award of DARPA RAM Cooperative Agreement N66001-14-2-4-032 to J.R.M. The  
474 content is solely the responsibility of the authors and does not necessarily represent the official views of our  
475 supporting organizations.

476 **Author contributions**

477 Concept: J.R.M. Implementation: T.H.C., L.L.W.O., and J.R.M. Analyses: L.L.W.O and J.R.M.

478 **References**

- 479 Alvarez-Hamelin, I., Dall'Asta, L., Barrat, A., & Vespignani, A. (2005). *k*-corr decomposition: a tool for the  
480 visualization of large scale networks. *arXiv*, cs/0504107v2.
- 481 Barthélemy, M. (2004). Betweenness centrality in large complex networks. *European Physical Journal B*, 38,  
482 163–168.
- 483 Bassett, D., Meyer-Lindenberg, A., Achard, S., Duke, T., & Bullmore, E. (2006, December). Adaptive  
484 reconfiguration of fractal small-world human brain functional networks. *Proceedings of the National  
485 Academy of Sciences, USA*, 103(51), 19518–23.
- 486 Bonacich, P. (2007). Some unique properties of eigenvector centrality. *Social Networks*, 29(4), 555–564.
- 487 Bullmore, E., & Sporns, O. (2009). Complex brain networks: graph theoretical analysis of structural and  
488 functional systems. *Nature Reviews Neuroscience*, 10(3), 186–198.
- 489 Capota, M., Turek, J., Chen, P.-H., Zhu, X., Manning, J. R., Sundaram, N., . . . Shin, Y. S. (2017). *Brain imaging  
490 analysis kit*. Retrieved from <https://doi.org/10.5281/zenodo.59780>
- 491 Christakis, N. A., & Fowler, J. H. (2010). Social network sensors for early detection of contagious outbreaks.  
492 *PLoS One*, 5(9), e12948.

- 493 Combrisson, E., Vallat, R., O'Reilly, C., Jas, M., Pascarella, A., l Saive, A., ... Jerbi, K. (2019). Visbrain: a  
494 multi-purpose GPU-accelerated open-source suite for multimodal brain data visualization. *Frontiers in*  
495 *Neuroinformatics*, 13(14), 1–14.
- 496 Comon, P., Jutten, C., & Herault, J. (1991). Blind separation of sources, part II: Problems statement. *Signal*  
497 *Processing*, 24(1), 11 - 20.
- 498 Demertzi, A., Tagliazucchi, E., Dehaene, S., Deco, G., Barttfeld, P., Raimondo, F., ... Sitt, J. D. (2019). Human  
499 consciousness is supported by dynamic complex patterns of brain signal coordination. *Science Advances*,  
500 5(2), eaat7603.
- 501 Estrada, E., & Rodríguez-Velázquez, J. A. (2005). Subgraph centrality in complex networks. *Physical Review*  
502 *E*, 71(5), 056103.
- 503 Etzel, J. A., Gazzola, V., & Keysers, C. (2009). An introduction to anatomical ROI-based fMRI classification.  
504 *Brain Research*, 1282, 114–125.
- 505 Fong, A. H. C., Yoo, K., Rosenberg, M. D., Zhang, S., Li, C.-S. R., Scheinost, D., ... Chun, M. M. (2019).  
506 Dynamic functional connectivity during task performance and rest predicts individual differences in  
507 attention across studies. *NeuroImage*, 188, 14–25.
- 508 Freeman, L. C. (1977). A set of measures of centrality based on betweenness. *Sociometry*, 40(1), 35–41.
- 509 Geisberger, R., Sanders, P., & Schultes, D. (2008). Better approximation of betweenness centrality. *Proceedings*  
510 *of the meeting on Algorithm Engineering and Experiments*, 90–100.
- 511 Gershman, S., Blei, D., Pereira, F., & Norman, K. (2011). A topographic latent source model for fMRI data.  
512 *NeuroImage*, 57, 89–100.
- 513 Halu, A., Mondragón, R. J., Panzarasa, P., & Bianconi, G. (2013). Multiplex PageRank. *PLoS One*, 8(10),  
514 e78293.
- 515 Haxby, J. V., Gobbini, M. I., Furey, M. L., Ishai, A., Schouten, J. L., & Pietrini, P. (2001). Distributed and  
516 overlapping representations of faces and objects in ventral temporal cortex. *Science*, 293, 2425–2430.
- 517 Hinton, G. E., & Salakhutdinov, R. R. (2006). Reducing the dimensionality of data with neural networks.  
518 *Science*, 313(5786), 504–507.
- 519 Honey, C. J., Kötter, R., Breakspear, M., & Sporns, O. (2007). Network structure of cerebral cortex shapes  
520 functional connectivity on multiple time scales. *Proceedings of the National Academy of Science USA*, 104(24),  
521 10240–10245.

- 522 Huth, A. G., de Heer, W. A., Griffiths, T. L., Theunissen, F. E., & Gallant, J. L. (2016). Natural speech reveals  
523 the semantic maps that tile human cerebral cortex. *Nature*, 532, 453–458.
- 524 Huth, A. G., Nisimoto, S., Vu, A. T., & Gallant, J. L. (2012). A continuous semantic space describes  
525 the representation of thousands of object and action categories across the human brain. *Neuron*, 76(6),  
526 1210–1224.
- 527 Jutten, C., & Herault, J. (1991). Blind separation of sources, part I: An adaptive algorithm based on  
528 neuromimetic architecture. *Signal Processing*, 24(1), 1–10.
- 529 Kamitani, Y., & Tong, F. (2005). Decoding the visual and subjective contents of the human brain. *Nature  
530 Neuroscience*, 8, 679–685.
- 531 Landau, E. (1895). Zur relativen Wertbemessung der Turnierresultate. *Deutsches Wochenschach*, 11, 366–369.
- 532 Lee, D. D., & Seung, H. S. (1999). Learning the parts of objects by non-negative matrix factorization. *Nature*,  
533 401, 788–791.
- 534 Lin, J. (2009). Divergence measures based on the Shannon entropy. *IEEE Transactions on Information Theory*,  
535 37(1), 145–151.
- 536 Lohmann, G., Margulies, D. S., Horstmann, A., Pleger, B., Lepsien, J., Goldhahn, D., ... Turner, R. (2010).  
537 Eigenvector centrality mapping for analyzing connectivity patterns in fMRI data of the human brain.  
538 *PLoS One*, 5(4), e10232.
- 539 Mairal, J., Ponce, J., Sapiro, G., Zisserman, A., & Bach, F. R. (2009). Supervised dictionary learning. *Advances  
540 in Neural Information Processing Systems*, 1033–1040.
- 541 Mairal, J. B., Bach, F., Ponce, J., & Sapiro, G. (2009). Online dictionary learning for sparse coding. *Proceedings  
542 of the 26th annual international conference on machine learning*, 689–696.
- 543 Manning, J. R., Ranganath, R., Norman, K. A., & Blei, D. M. (2014). Topographic factor analysis: a Bayesian  
544 model for inferring brain networks from neural data. *PLoS One*, 9(5), e94914.
- 545 Manning, J. R., Zhu, X., Willke, T. L., Ranganath, R., Stachenfeld, K., Hasson, U., ... Norman, K. A. (2018).  
546 A probabilistic approach to discovering dynamic full-brain functional connectivity patterns. *NeuroImage*,  
547 180, 243–252.
- 548 McInnes, L., & Healy, J. (2018). t-SNE: Uniform manifold approximation and projection for dimension  
549 reduction. *arXiv*, 1802(03426).

- 550 Mitchell, T., Shinkareva, S., Carlson, A., Chang, K., Malave, V., Mason, R., & Just, M. (2008). Predicting  
551 human brain activity associated with the meanings of nouns. *Science*, 320(5880), 1191.
- 552 Newman, M. E. J. (2005). A measure of betweenness centrality based on random walks. *Social Networks*, 27,  
553 39–54.
- 554 Newman, M. E. J. (2008). The mathematics of networks. *The New Palgrave Encyclopedia of Economics*, 2, 1–12.
- 555 Nishimoto, S., Vu, A., Naselaris, T., Benjamini, Y., Yu, B., & Gallant, J. (2011). Reconstructing visual  
556 experience from brain activity evoked by natural movies. *Current Biology*, 21, 1 - 6.
- 557 Nocedal, J., & Wright, S. J. (2006). *Numerical optimization*. New York: Springer.
- 558 Norman, K. A., Newman, E., Detre, G., & Polyn, S. M. (2006). How inhibitory oscillations can train neural  
559 networks and punish competitors. *Neural Computation*, 18, 1577–1610.
- 560 Opsahl, T., Agneessens, F., & Skvoretz, J. (2010). Node centrality in weighted networks: generalizing degree  
561 and shortest paths. *Social Networks*, 32, 245–251.
- 562 Pearson, K. (1901). On lines and planes of closest fit to systems of points in space. *The London, Edinburgh,*  
563 *and Dublin Philosophical Magazine and Journal of Science*, 2, 559-572.
- 564 Pereira, F., Lou, B., Pritchett, B., Ritter, S., Gershman, S. J., Kanwisher, N., ... Fedorenko, E. (2018). Toward  
565 a universal decoder of linguistic meaning from brain activation. *Nature Communications*, 9(963), 1–13.
- 566 Rao, C. R. (1982). Diversity and dissimilarity coefficients: a unified approach. *Theoretical Population Biology*,  
567 21(1), 24–43.
- 568 Ricotta, C., & Szeidl, L. (2006). Towards a unifying approach to diversity measures: Bridging the gap  
569 between the Shannon entropy and Rao's quadratic index. *Theoretical Population Biology*, 70(3), 237–243.
- 570 Rubin, T. N., Kyoejo, O., Gorgolewski, K. J., Jones, M. N., Poldrack, R. A., & Yarkoni, T. (2017). Decoding  
571 brain activity using a large-scale probabilistic functional-anatomical atlas of human cognition. *PLoS*  
572 *Computational Biology*, 13(10), e1005649.
- 573 Rubinov, M., & Sporns, O. (2010). Complex network measures of brain connectivity: uses and interpreta-  
574 tions. *NeuroImage*, 52, 1059–1069.
- 575 Schreiber, T. (2000). Measuring information transfer. *Physical Review Letters*, 85(2), 461–464.
- 576 Simony, E., Honey, C. J., Chen, J., & Hasson, U. (2016). Uncovering stimulus-locked network dynamics  
577 during narrative comprehension. *Nature Communications*, 7(12141), 1–13.

- 578 Spearman, C. (1904). General intelligence, objectively determined and measured. *American Journal of*  
579 *Psychology*, 15, 201–292.
- 580 Sporns, O., & Honey, C. J. (2006). Small worlds inside big brains. *Proceedings of the National Academy of*  
581 *Science USA*, 103(51), 19219–19220.
- 582 Tipping, M. E., & Bishop, C. M. (1999). Probabilistic principal component analysis. *Journal of Royal Statistical*  
583 *Society, Series B*, 61(3), 611–622.
- 584 Tong, F., & Pratte, M. S. (2012). Decoding patterns of human brain activity. *Annual Review of Psychology*, 63,  
585 483–509.
- 586 Turk-Browne, N. B. (2013). Functional interactions as big data in the human brain. *Science*, 342, 580–584.
- 587 van der Maaten, L. J. P., & Hinton, G. E. (2008). Visualizing high-dimensional data using t-SNE. *Journal of*  
588 *Machine Learning Research*, 9, 2579-2605.
- 589 Zar, J. H. (2010). *Biostatistical analysis*. Prentice-Hall/Pearson.